St. Joseph's Journal of Humanities and Science
ISSN: 2347 - 5331
http://sjctnc.edu.in/6107-2/


# Structural, Functional and Optical Characters of $TiO_2$ Nanocrystallites: Anatase and Rutile Phases

**P. Praveen[a*]**
**G. Viruthagiri[b]**
**S. Mugundan[c]**
**M. Jothibas[d]**
**M. Prakash[c]**
**R. Sagayaraj[a]**

## ABSTRACT

The anatase and rutile phases of titania ($TiO_2$) nanoparticles were synthesized by Sol–gel technique at room temperature with appropriate reactants. The XRD patterns confirmed the tetragonal crystal structure and the structural properties were determined. The relative functional groups and purity of the prepared products were identified by FTIR spectroscopy. DRS measurements indicated that the blue shift in the absorption band edges with respect to bulk titania. The allowed direct and indirect band gap energies, as well as the optical constants were evaluated.

**Keywords:** Sol-gel technique; $TiO_2$ nanoparticles; X-ray diffraction; Functional groups; Optical properties.

## INTRODUCTION

Titania ($TiO_2$) has been widely studied due its interesting properties such as high dielectric constant, humidity and oxygen sensitivities and, photoelectric and catalytic conversion properties [1, 2]. Titania crystallizes in three natural phases: brookite (orthorhombic), anatase (tetragonal) and rutile (tetragonal). The brookite and anatase crystalline phases, which are stable at low temperature, transform into rutile when the sample is annealed at higher temperatures [3]. It has been demonstrated that some properties of $TiO_2$ are very sensitive to its structure. Since the anatase phase is chemically and optically active, it is suitable for catalysts and supports [4, 5]. On the other hand, the rutile phase has the highest refractive index and ultraviolet absorptivity among the titania phases; thus, it is employed in pigments, paints and ultraviolet absorbents [4]. According to the temperature, the anatase-rutile transformation is

[a]PG and Research Department of Physics, St. Joseph's College of Arts & Science (Autonomous), Cuddalore-607001, Tamil Nadu.
[b]Department of Physics, Annamalai University, Annamalai Nagar-608002, Tamil Nadu, India.
[c]Sri Vijay Vidyalaya College of Arts & Science (Women's), Dharmapuri-636807, Tamil Nadu, India.
[d]Department of Physics, T.B.M.L. College, Porayar-609307, Tamil Nadu, India.
[e]Department of Physics, Urumu Dhanalakshmi College, Tiruchirappalli-620019, Tamil Nadu, India.
*E-mail: drdhanapriyan@gmail.com.

related to some extent with the degree of packing of the particles, since the transformation begins with the nucleation of rutile on anatase and the rutile nuclei grow throughout the anatase particle until completion [4]. High surface area titania is commonly formed by the metastable anatase phase which upon heating at temperatures above 800 K, transforms into the more stable rutile form with extensive surface area loss [4, 5]. Since anatase is a metastable $TiO_2$ polymorph, it tends to transform into the rutile phase, decreasing the surface area, inducing a loss of catalytic activity [6, 7]. Rutile is much closer to aromatic packing in its crystal pattern, and it is more stable than anatase phase. The denser atomic crystal pattern of rutile $TiO_2$ causes it to have higher specific gravity and refractive index than the anatase phase. In recent years, nano-$TiO_2$ material has attracted researchers, owing to improved optical property [8], photo catalytic action [9], and other special characteristics to coating [10–13]. The nano-$TiO_2$ incorporated composite coatings considerably improve the mechanical properties and enhance the thermal stability [14, 15].

In the earlier reports, the synthesis [16], structure and morphology [17, 18], crystallization and phase transformation [19, 20], metals doped rutile $TiO_2$ [7], [21, 22] and some applications like lithium-ion batteries [23], Superhydrophobic, UV-Shielding and Self-Cleaning properties [24] are discussed. The spectral, tensor, and ab initio theoretical analysis of optical second harmonic generation from the rutile $TiO_2$ (110) and (001) faces are performed by Omote et al., (2005) [25]. In our earlier works, the preparation and properties of sol-gel derived pure [26] and transition metal elements (such as Mn, Fe, Cu, Ag, Ni and Co) doped $TiO_2$ nanoparticles have been analyzed [27–32]. Herein, we report on the synthesis, structural, functional and optical analyses of anatase and rutile $TiO_2$ nanoparticles.

## EXPERIMENTAL SECTION

### Sol-gel synthesis of $TiO_2$ nanoparticles

All chemical reagents used in the present study were obtained from commercial sources as analytical reagent (AR) grade and used without any further purification. In a typical synthesis, 10 ml of tetra-isopropyl orthotitanate ($Ti(OPr^i)_4$, TIOT, assay ≥ 98%) was dissolved in 90 ml of isopropyl alcohol ($(CH_3)_2$•CHOH, assay >99%) and to this solution 5 ml of deionized water was added drop wise with vigorous magnetic stirring. The resulting colloidal suspension was stirred for 4h at room temperature. The obtained gel was filtered by Whatman filter paper (110 mm Ø) and washed several times using ethanol and deionized water. The yield gel was dried in a hot air oven at 100°C for 6h to evaporate water and organic material to the maximum extent. Then, the dried powder was ground by agate mortar using pestle to avoid agglomerates. Finally, the powder was kept into muffle furnace and annealed at 450°C (for anatase) and 750°C (for rutile) for 4h each, subsequently carried out to obtain desired phase pure $TiO_2$ nanocrystallites. After the annealing process, the pure $TiO_2$ has white in both anatase and rutile phases. The annealed products were pulverized into fine powders using mortar for further characterizations.

### Characterizations

The crystalline phase and particle size of pure $TiO_2$ nanoparticles were analyzed by X-ray diffraction (XRD) measurement which was carried out at room temperature by using XPERT-PRO diffractometer system (scan step of 0.05° (2θ), counting time of 10.16 s per data point) equipped with a Cu tube for generating CuKα radiation (λ = 1.5406 Å); as an incident beam in the 2-theta mode over the range of 10°-80°, operated at 40 kV and 30 mA. The vibrational assignments were identified by AVATAR 330 Fourier transform infrared (FTIR) spectrophotometer in which the IR spectra were recorded by diluting the milled powders in KBr and in the wavelength between 4000-400 $cm^{-1}$. The band gap energies were measured at wavelength in the range of 200-800 nm by UV-Vis-NIR spectrophotometer (Varian/Carry 5000) equipped with an integrating sphere and the baseline correction was performed using a calibrated reference sample of powdered barium sulfate ($BaSO_4$).

## RESULTS AND DISCUSSION

### X-ray diffraction analysis

Fig.1 shows the powder X-ray diffraction patterns of anatase and rutile $TiO_2$ nanoparticles derived from sol-gel route by the heat treatment at 450 and 750°C,

respectively. In Fig.1(a), the XRD pattern revealed the reflections corresponding to the anatase phase (JCPDS: 21-1272) [26].

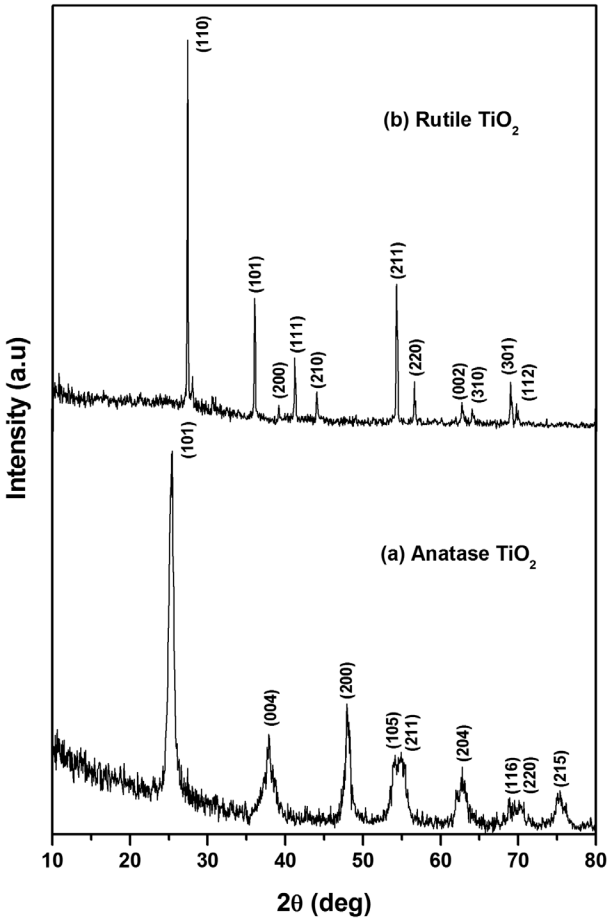


**Figure 1: X-ray diffractograms of (a) anatase and (b) rutile $TiO_2$ nanoparticles.**

This indicates that the amorphous $TiO_2$ crystallized in anatase phase at 450°C. It was reported that the anatase to rutile transformation in the annealing process does not occur at temperatures below 600°C [33]. After annealing at 750°C, the relative intensity of the anatase peaks with respect to rutile peaks were vanished (Fig.1-b). Therefore, practically only the peaks assigned to the rutile phase was observed, indicating a complete phase transformation from anatase to rutile at this temperature. The as-prepared $TiO_2$ powder was found to be amorphous; it was reported in earlier literature [19]. In Fig.1-b, all peaks were indexed within the tetragonal structure of rutile phase which crystal structure was formed by corner-bonded ($TiO_6$) octahedra (JCPDS: 21-1276). However, the intensity of rutile XRD peaks appeared sharper when comparison with the broader anatase peaks. The crystallite size has been obtained from 2θ and the full width at half maximum (FWHM) of the (h k l) peaks using Scherrer's relation [34],

$$D = \frac{K\lambda}{\beta Cos\theta}\ \dot{A}$$

where D is the average crystallite size in Å, K is the shape factor (0.9), λ is the wavelength of X-ray (1.5406 Å) CuKα radiation, θ is the Bragg angle and β is the corrected line broadening of the nanoparticles. By applying Scherrer's formula on the anatase and rutile diffraction peaks, the average crystallite sizes were found to be 15.31 and 70.96 nm (Table 1), respectively. Hence, the $TiO_2$ crystallite size was increased with high annealing temperature. The lattice constants 'a' and 'c' for the tetragonal structure ($a = b \neq c$, $\alpha = \beta = \gamma = 90.0°$) can be calculated by the following expression [35],

$$Sin^2\theta = \frac{\lambda^2(h^2 + k^2)}{4a^2} + \frac{\lambda^2(l^2)}{4c^2}\ \dot{A}$$

where h, k and l are the Miller indices of the peak. From the values of 'a' and 'c', the unit cell volume ($V = a^2c$) can be determined. Hence, the standard JCPDS of anatase (21-1272) and rutile (21-1276) $TiO_2$ are good agreement with the recorded XRD patterns. The calculated results are shown in Table 2. The structural parameters are calculated from the following equations [36, 37],

$$\textbf{Dislocation density, } \delta = \frac{1}{D^2}$$

$$\textbf{Micro strain, } \varepsilon = \frac{\beta \cos\theta}{4}$$

$$\textbf{Stacking fault, } SF = \left[\frac{2\pi^2}{45(3\tan\theta)^{1/2}}\right]\beta$$

$$\textbf{Texture co-efficient, } TC(hkl) = \frac{I(hkl)/I_0(hkl)}{\sum I(hkl)/I_0(hkl)} \times 100\%$$

**Table 1: Structural properties of $TiO_2$ nanoparticles**

| $TiO_2$ Phase | 2θ deg | FWHM | d (Å) | (hkl) | D (nm) | δ ($\times10^{15}$) | ε ($\times10^{-3}$) | SF ($\times10^{-3}$) | TC | n |
|---|---|---|---|---|---|---|---|---|---|---|
| Anatase (Annealed @ 450°C) | 25.28 | 0.68 | 3.52 | (101) | 11.97 | 6.9792 | 2.8949 | 6.3041 | 1.2586 | 25573 |
| | 37.81 | 0.35 | 2.38 | (004) | 23.99 | 1.7375 | 1.4446 | 2.6408 | 0.7060 | 205871 |
| | 47.99 | 0.60 | 1.89 | (200) | 14.48 | 4.7693 | 2.3915 | 3.9709 | 1.0745 | 45270 |
| | 53.95 | 0.40 | 1.70 | (105) | 22.28 | 2.0145 | 1.5554 | 2.4756 | 0.6205 | 164911 |
| | 55.00 | 1.00 | 1.67 | (211) | 8.95 | 12.4840 | 3.8702 | 6.1199 | 0.5273 | 10689 |
| | 62.90 | 0.60 | 1.47 | (204) | 15.52 | 4.1516 | 2.2331 | 3.3876 | 0.6203 | 55741 |
| | 75.00 | 1.00 | 1.26 | (215) | 10.01 | 9.9800 | 3.4614 | 5.0407 | 0.9754 | 14955 |
| Rutile (Annealed @ 750°C) | 27.35 | 0.11 | 3.25 | (110) | 69.69 | 0.2059 | 0.4663 | 0.9846 | 1.1403 | 5647625 |
| | 35.99 | 0.12 | 2.49 | (101) | 69.42 | 0.2075 | 0.4979 | 0.9296 | 0.9763 | 5582237 |
| | 39.10 | 0.11 | 2.30 | (200) | 76.44 | 0.1711 | 0.4522 | 0.8151 | 0.7469 | 7452749 |
| | 41.16 | 0.11 | 2.19 | (111) | 76.93 | 0.1689 | 0.4493 | 0.7926 | 0.8922 | 7596992 |
| | 43.99 | 0.12 | 2.05 | (210) | 71.20 | 0.1972 | 0.4854 | 0.8337 | 1.1107 | 6022745 |
| | 54.25 | 0.12 | 1.68 | (211) | 74.18 | 0.1817 | 0.4660 | 0.7403 | 1.0854 | 6811064 |
| | 56.57 | 0.11 | 1.62 | (220) | 81.79 | 0.1494 | 0.4226 | 0.6621 | 0.8541 | 9129670 |
| | 62.67 | 0.16 | 1.48 | (002) | 57.98 | 0.2974 | 0.5962 | 0.9054 | 0.7685 | 3252288 |
| | 64.01 | 0.16 | 1.45 | (310) | 58.39 | 0.2933 | 0.5920 | 0.8936 | 0.4128 | 3321772 |
| | 68.94 | 0.15 | 1.36 | (301) | 64.07 | 0.2436 | 0.5395 | 0.7993 | 0.8552 | 4388525 |
| | 69.72 | 0.12 | 1.34 | (112) | 80.46 | 0.1544 | 0.4296 | 0.6348 | 0.8866 | 8691496 |

**Table 2: Evaluated crystal parameters for $TiO_2$ nanoparticles with reference of JCPDS Cards (Anatase: 21-1272; Rutile: 21-1276)**

| $TiO_2$ Phase | Crystal structure | Space group | Lattice parameters (Å) | | | | Volume V (Å$^3$) | |
|---|---|---|---|---|---|---|---|---|
| | | | Calculated | | JCPDS | | Calculated | JCPDS |
| | | | a | c | a | c | | |
| *Anatase* | *Tetragonal* | $I4_1/amd$ | 3.788 | 9.513 | 3.785 | 9.513 | 136.51 | 136.31 |
| *Rutile* | | $P4_2/mnm$ | 4.600 | 2.960 | 4.593 | 2.959 | 62.63 | 62.43 |

The structural parameters including crystallite size, dislocation density, micro strain, stacking fault and texture co-efficient of anatase and rutile $TiO_2$ nanoparticles are summarized in Table 1. The lattice defects like dislocation density (δ), micro strain (ε) and stacking fault (SF) showed a decreasing trend with increasing temperature from 450 to 750°C which may be due to the improvement of crystallinity as well as the high orientation along (110) direction (Fig.1-b). The minimum values of δ and ε which lead to the carriers to move freely in the lattice. It was generally observed that the δ and ε in the nanoparticles decreases as the crystallite size increases which is a well-known phenomenon [38]. The texture co-efficient (TC) represents the texture of a particular plane. Quantitative information concerning the preferential crystallite orientation was obtained from TC(hkl). Where I(hkl) is the measured relative intensity of a plane (hkl) and $I_0$(hkl) is the standard intensity of the plane taken from the JCPDS data. The value TC(hkl) = 1 represents randomly oriented crystallite, while higher values indicate the abundance of grains oriented in a given (hkl) direction. Hence, the TC clearly indicates that the anatase and rutile $TiO_2$ are highly oriented in (101) and (110) directions, respectively. The nanoparticle formation takes place due to agglomeration of the primary particles, which in this case is the single $TiO_2$ unit. Agglomeration number specifies the number of primary particles or molecules contained in a single nanoparticle of a given size [39]. Assuming the nanoparticles to be exactly spherical and also evident from SEM (Fig.10), particle agglomeration number was calculated from the following expression [40, 41],

$$\text{Agglomeration number, } n = \frac{4\pi N_a r^3}{3V_m}$$

where, n is the agglomeration number, $N_a$ is Avogadro's number ($6.02\times10^{23}$), $V_m$ is the molar volume of $TiO_2$ (anatase: 21.13; rutile: 18.88) in cm$^3$ mol$^{-1}$ and r is the nanoparticle radius. From the Table 1, the lowest value of agglomeration number is predicted for the anatase phase confirming its lower particle size with minimum agglomeration.

## 3.2 Functional Group Analysis

Fig.2 depicts the FTIR spectra of the anatase and rutile $TiO_2$ nanoparticles annealed at 450 and 750°C, respectively along with of as-prepared (dried at 100°C) $TiO_2$ sample. The reaction between precursor materials of $TiO_2$ has resulted in the white powdered products that invariably found for three different temperatures. For the as-prepared $TiO_2$ (Fig.2-a), several absorption bands correspond to the vibrational modes of organic species such as hydroxyl, carboxilate and alkane groups were observed. A broad band observed at 3443.66 cm$^{-1}$ was related to the O–H stretching mode of hydroxyl group, indicating the presence of moisture in the sample [19]. The peak at 1631.84 cm$^{-1}$ was attributed to O-H bending vibration. The peaks in between 2923.64 and 2853.78 cm$^{-1}$ could be ascribed to the characteristic frequencies of residual organic species are assigned to C–H stretching vibrations of alkane groups. The peaks at 1747.95 and 1741.99 cm$^{-1}$ can be associated to the asymmetric stretching mode of titanium carboxilate. The strong absorption band observed at 537.22 cm$^{-1}$ can be attributed to the Ti-O bond.

For anatase and rutile $TiO_2$ nanoparticles (Fig.2-b,c), the spectroscopic band was observed in the range 3391.72-3390.48 cm$^{-1}$, which is described to the both symmetric and asymmetric stretching vibrations of the hydroxyl group (Ti–OH). Whereas, the characteristic peaks between 1630.69 and 1627.28 cm$^{-1}$ were associated

with the O–H bending vibration of the absorbed water molecules [42]. Furthermore, the spectra reveal that the peak at 463.88 $cm^{-1}$ should be attributed to Ti–O bond in the $TiO_2$ lattice (anatase titania). However, the metal oxide $TiO_2$ was formed by thermolysis of the powderd products [43]. The peak at 536.99 $cm^{-1}$ indicates the metal-oxygen (Ti-O) bond and the broad band located in the region 728.77 and 645.99 $cm^{-1}$ illustrates the Ti-O-Ti bond. Two weak bands between 2926.03-2920.55 $cm^{-1}$ and 2849.33 $cm^{-1}$ could be assigned to C–H stretching vibrations. The peaks at 1383.04 and 1342.47 $cm^{-1}$ region could be attributed to carboxyl (C=O) and methylene groups. On annealing at 450 and 750°C, the intensity of the bands associated with the organic groups decreased significantly (Fig.2-b,c), indicating the elimination of organic species from the samples. On the other hand, the FTIR spectra of as-prepared and anatase $TiO_2$ samples revealed peaks at about 1462.00, 1383.04 and 1342.47 $cm^{-1}$ (Fig.2-a,b), which were not observed for the rutile $TiO_2$ (Fig.2-c). Thus, indicate that the improved phase purity and crystallinity were observed after the annealing treatment.

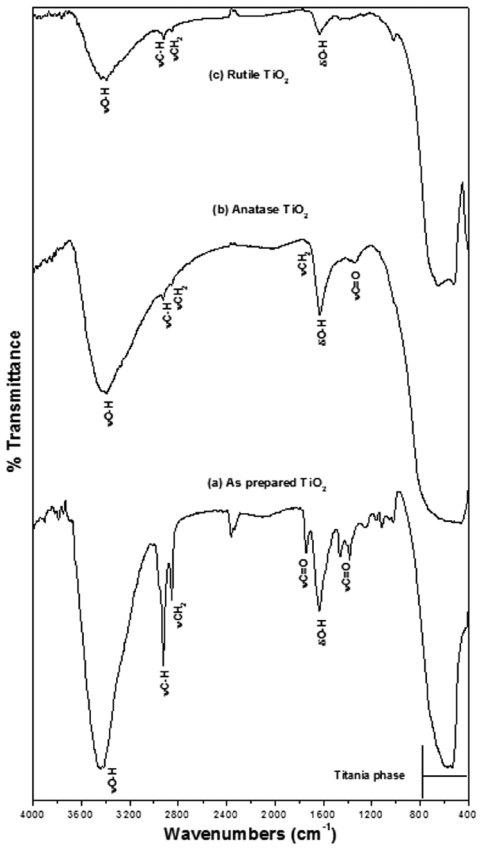


**Figure 2: FTIR spectra of (a) as-prepared (100°C), (b) anatase (450°C) and (c) rutile (750°C) $TiO_2$ nanoparticles.**

The anatase and rutile $TiO_2$ nanoparticles prepared for the present study are of good quality and can be used for the further characterizations. The infrared absorption frequencies and the corresponding functional groups are represented in Table 3.

**Table 3: The Vibrational Assignment of $TiO_2$ Nanostructures**

| Wavenumbers ($cm^{-1}$) | | | Tentative vibrational assignments |
|---|---|---|---|
| As-prepared $TiO_2$ | Anatase $TiO_2$ | Rutile $TiO_2$ | |
| 3443.66 | 3391.72 | 3390.48 | O-H stretching |
| 2923.64 | 2920.55 | 2926.03 | C-H stretching |
| 2853.78 | 2849.32 | 2849.32 | |
| 1741.99 | 1747.95 | - | C=O stretching |
| 1631.84 | 1627.28 | 1630.69 | O-H bending |
| 1462.00 | - | - | Carboxyl and methylene groups |
| 1383.04 | 1342.47 | - | |
| - | 728.77 | 645.99 | Ti-O-Ti bond |
| 537.22 | - | 536.99 | Ti-O bond |
| - | 463.88 | - | Anatase titania |

## Linear optical study

### *Determination of band gap energy*

The diffuse reflectance spectra of anatase and rutile $TiO_2$ nanoparticles were illustrated in Fig.3. Compared with bulk $TiO_2$ [44], the absorption edges of both phases of nano-titania were shifted towards the higher energy region. The band gap energy ($E_g$) was obtained from the direct energy equation [45].

$$E_g = \frac{hc}{\lambda} eV$$

where h is the Planck's constant ($6.626\times10^{-34}$ Js), c is the light velocity ($3\times10^8$ m/s) and λ is the wavelength (nm). The absorption edge of nano-anatase was at 345 nm corresponding to $E_g$ of 3.58 eV, whereas nano-rutile has absorption edge at 380 nm with $E_g$ of 3.25 eV.

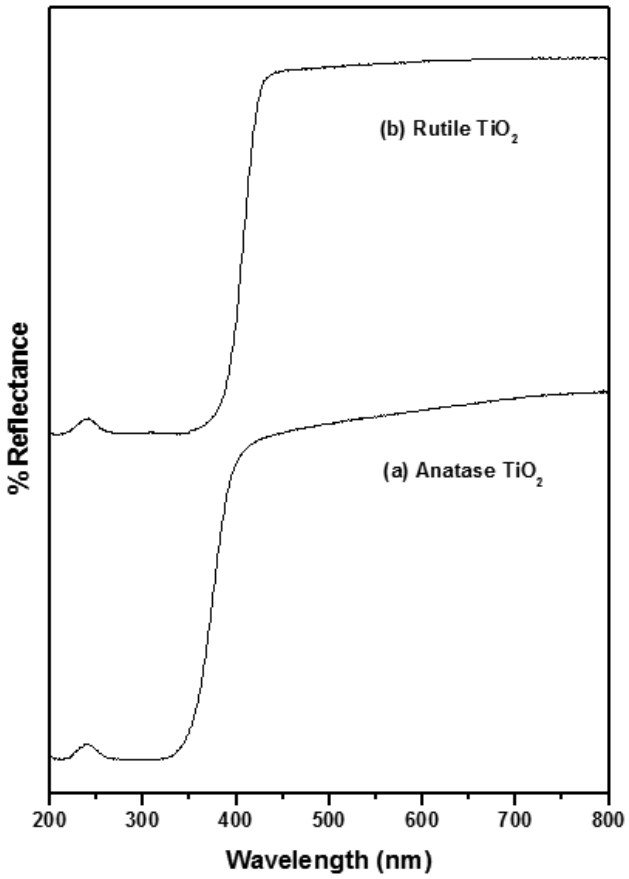


**Figure 3: UV-Vis-DRS spectra of (a) anatase and (b) rutile $TiO_2$ nanoparticles**

Hence, it can be clearly seen that the band gap energies of both anatase and rutile $TiO_2$ nanoparticles were higher than that of bulk (anatase: 3.2 eV; rutile: 3.02 eV) $TiO_2$ [44].

***Allowed direct and indirect band gap energy***

The absorption edges of nano – anatase and rutile $TiO_2$ were blue-shifted about 40 and 30 nm, compared with that of respective bulk titania [44]. The allowed direct band gap energy can be estimated from the plots of $(\alpha h\nu)^2$ vs. photon energy ($h\nu$) by using the relationship

$$\alpha h\nu = A(h\nu - E_g)^n$$

The optical absorbance co-efficient ($\alpha$) of a semiconductor close to the band edge can be expressed by the following equation,

$$\alpha = A(h\nu - E_g)^n / h\nu$$

In this case n=1/2 for the allowed direct transition. The plots of $(\alpha h\nu)^2$ vs. $h\nu$ was presented in Fig.4. The direct band gap energies of anatase and rutile $TiO_2$ nanoparticles were calculated to be 3.58 and 3.23 eV (Table 4), respectively. Meanwhile, the crystallite sizes were 15.31 and 70.96 nm, respectively for anatase and rutile $TiO_2$ (from XRD). Thus indicates that the band gap energy increases with decreasing particle size due to quantum confinement effect [46]. Considering the blue shift of the absorption positions from the bulk $TiO_2$, the absorption onset of the materials can be assigned to the direct transition of electrons in the $TiO_2$ nanocrystals. The allowed indirect band gap energy of anatase and rutile $TiO_2$ nanoparticles can be estimated from plots of the square root of Kubelka–Munk (K-M) functions F(R) vs. $h\nu$. The reflectance data was converted to the absorption co-efficient F(R) values according to the K–M equation [47],

$$F(R)_{KM} = (1-R)^2 / 2R$$

where $F(R)_{KM}$ is equivalent to the absorption co-efficient ($\alpha_{KM}$), which can be expressed as,

$$\alpha_{KM} = (h\nu) = C_1(h\nu - E_g)^2$$

In this case n=2 for the allowed indirect transition. The Fig.5 shows the plots of K-M functions vs. $h\nu$. The anatase $TiO_2$ has an indirect band gap of 3.58 eV, while rutile exhibits 3.23 eV (Table 4) when the absorption edges shift from 385 to 345 nm and from 410 to 380 nm (Fig.3), respectively. This result is consistent with the fact that the conduction band edges of nano – anatase and rutile $TiO_2$ are about 0.38 and 0.21 eV more positive than that of respective bulk $TiO_2$ [44]. It is evident that $TiO_2$ shows large optical absorbance in the UV region.

***Evaluation of optical constants***

The extinction co-efficient (k) can be obtained from the relation [48],

$$\mathbf{k = \frac{\alpha\lambda}{4\pi}}$$

where $\alpha$ is the absorption co-efficient. Fig.6 depicted the variation of extinction co-efficient (k) values for anatase and rutile $TiO_2$ nanoparticles with wavelength. It has been found that $k_{max}$ values varying in the range of 0.15-0.29. Thus, the observed low $k_{max}$ value of these nanoparticles was a qualitative indication of surface smoothness and homogeneity of the $TiO_2$ materials [49]. From the Fig.6, the rapid decrease and increase k values are observed and are high in the UV region and low in the visible region. The rise and fall in the k value was directly related to absorption of light [50].

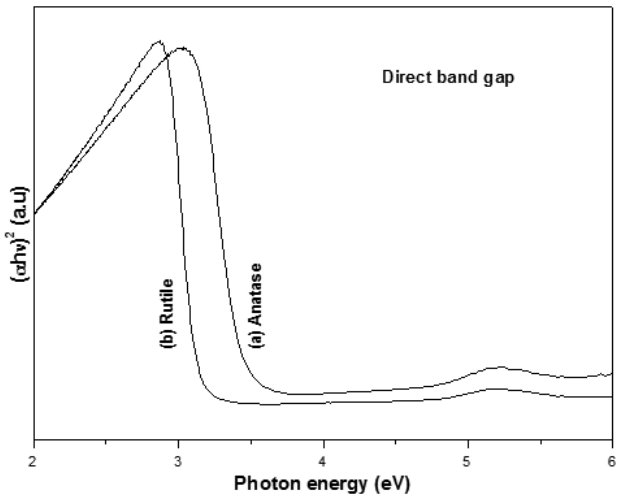


**Figure 4: Plot of direct band gap energy for (a) anatase and (b) rutile $TiO_2$ nanoparticles**

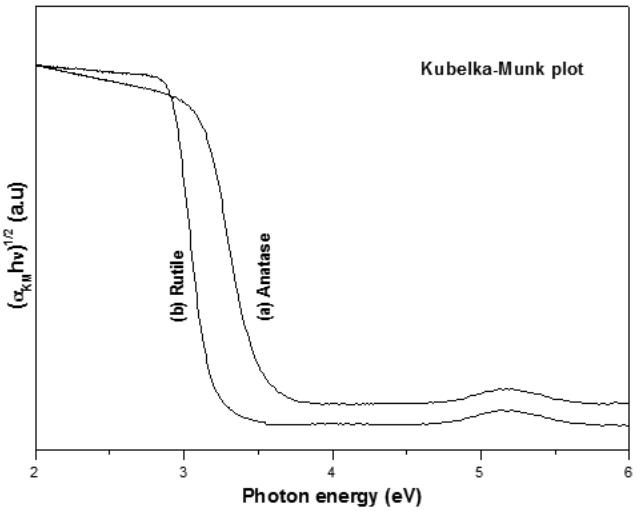


**Figure 5: Plot of indirect band gap energy for (a) anatase and (b) rutile $TiO_2$ nanoparticles**

**Table 4: Comparison of band gap energies and optical constants of different phases of $TiO_2$ nanoparticles**

| *$TiO_2$ Phase* | Band gap energy (eV) | | | | Extinction co-efficient (k) | Refractive index (n) | Dielectric constant (ε) | |
|---|---|---|---|---|---|---|---|---|
| | Bulk $TiO_2$ [44] | Nano $TiO_2$ | | | | | | |
| | | $E_g = h\nu$ | Allowed Direct | Allowed Indirect | | | $\varepsilon_1$ | $\varepsilon_2$ |
| *Anatase* | 3.2 | 3.58 | 3.58 | 3.58 | 0.15 | 2.56 | 6.59 | 0.65 |
| *Rutile* | 3.02 | 3.25 | 3.23 | 3.23 | 0.29 | 2.68 | 7.23 | 0.74 |

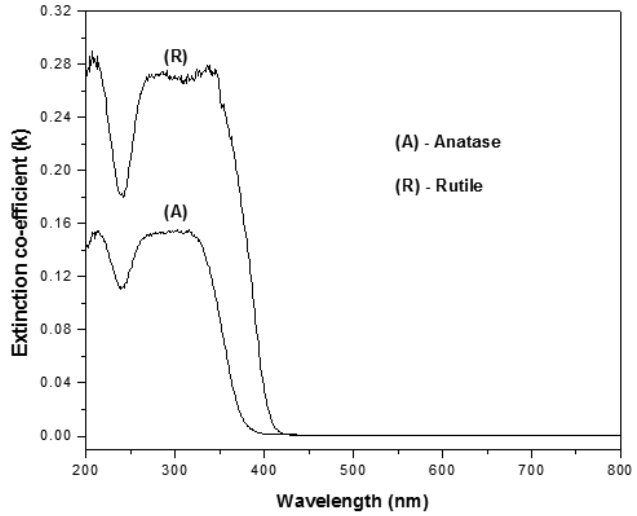


**Figure 6: Extinction co-efficient spectra of (A) anatase and (R) rutile $TiO_2$ nanoparticles**

Hence, it is concluded that the extinction co-efficient increases and shifts towards the higher wavelength side with high annealing temperature. The refractive index (n) was determined by using reflectance (R) and extinction co-efficient (k) data of the materials from the following expression [51],

$$n = \left[\frac{(1+R)}{(1-R)}\right] \pm \left\{\left[\frac{(1+R)}{(1-R)}\right]^2 - (1+K^2)\right\}^{1/2}$$

Fig.7 showed the variation of refractive index (n) of the anatase and rutile $TiO_2$ nanoparticles with different wavelengths. It is interesting to note that $n_{max}$ shifts to lower photon energy with the high annealing temperature and this shift corresponds to the temperature dependence of the energy band gap. From the Fig.7, it can be observed that the $n_{max}$ value of

$TiO_2$ was higher in the case of rutile phase and varying in the range 2.56–2.68. However, it is learnt that the refractive index increases in the UV region and rapidly decreases in the high transmission range. It is the most widely used physical quantity in optical design. The dielectric constant (ε) of the $TiO_2$ nanoparticles was calculated using the relation [52]

$$\varepsilon_1 = n^2 - k^2 \text{ and } \varepsilon_2 = 2nk$$

where $\varepsilon_1$ and $\varepsilon_2$ are the real and imaginary parts of the dielectric constant. The values of $\varepsilon_1$ and $\varepsilon_2$ for different incident photon energies can be obtained from the values of n and k by using the equations [53, 54]

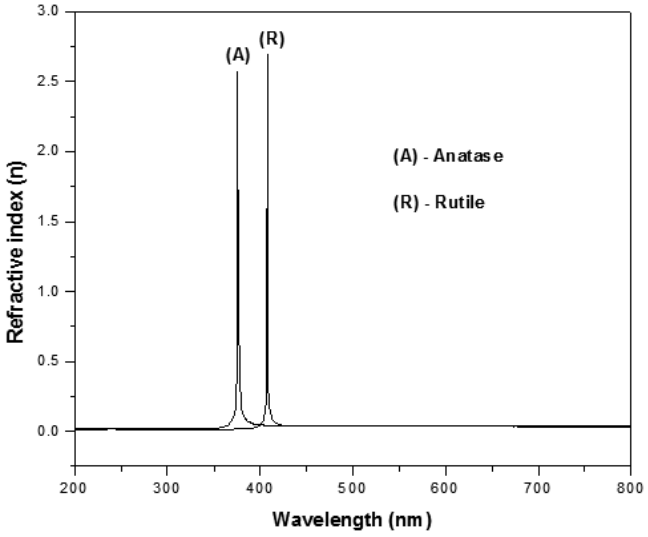


**Figure 7: Refractive index spectra of (A) anatase and (R) rutile $TiO_2$ nanoparticles**

The variation of the real and imaginary parts of the dielectric constant for anatase and rutile $TiO_2$ nanoparticles are illustrated in Figs.8-a,b. From these figures, it is observed that the values of the real part ($\varepsilon_1$) are higher than that of the imaginary part ($\varepsilon_2$). Moreover, the both $\varepsilon_1$ and $\varepsilon_2$ are always high in the UV region and low in the visible region. Due to higher annealing, the dielectric constants are shifted towards the higher wavelength side with increasing trend. The higher values of optical constants such as extinction co-efficient (k), refractive index (n) and dielectric constant (ε) are obtained for the rutile $TiO_2$ nanoparticles. The comparison of band gap energy measurements and optical constants of anatase and rutile $TiO_2$ nanoparticles are depicted in Table 4.

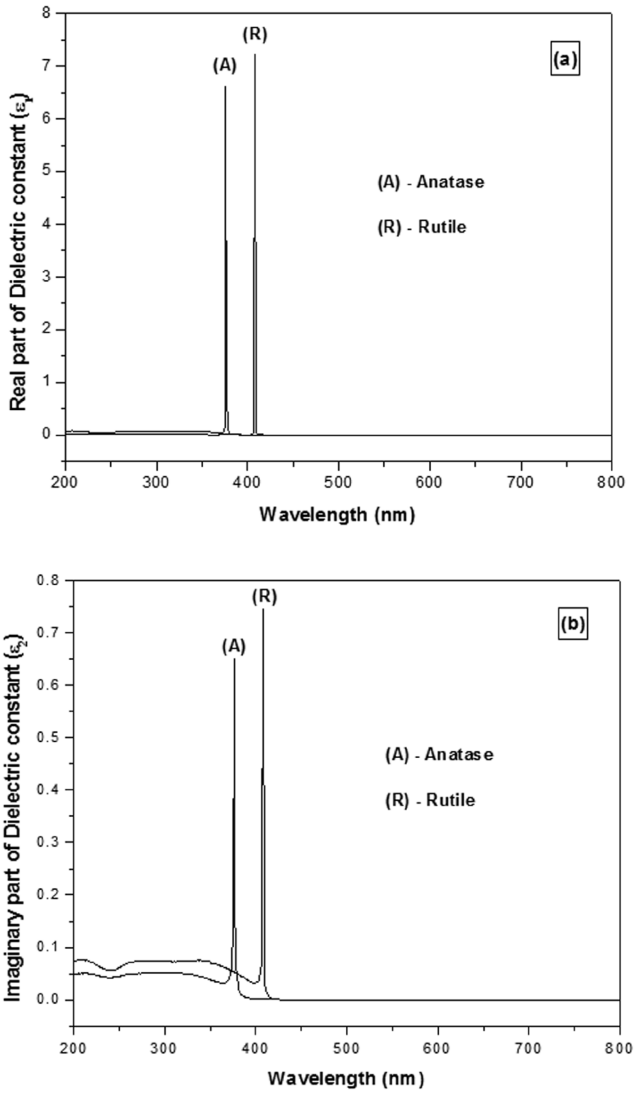


**Figure 8: (a) Real and (b) Imaginary parts of dielectric constants as a function of wavelength for (A) anatase and (R) rutile $TiO_2$ nanoparticles**

## CONCLUSIONS

The anatase and rutile phases of $TiO_2$ nanoparticles were successfully synthesized by sol-gel method. The XRD analysis reveals that the prepared products were attributed to the tetragonal crystal structure and preferentially oriented. In addition, the rutile $TiO_2$ has increased crystallite diameter and minimum lattice defects when compared to anatase titania. From the FTIR spectra, it can be realized that the phase purity of the samples was increased with annealing temperatures. The DRS analysis confirms that the absorption edge of rutile $TiO_2$ was red shifted with respect to the anatase phase. The comparison of allowed direct and indirect

band gap energies resulted the rutile has lower $E_g$ than that of anatase $TiO_2$. Moreover, the rutile titania has larger optical constants and are always high in the UV region and low in the visible region.

## REFERENCES


1. D. Bersani, P.P. Lottici, X.Z. Ding, Appl. Phys. Lett., 72 (1998)73-75.
2. J.E.G.J. Wijnhiven, W.L. Vos, Science, 281 (1998) 802-804.
3. X. Bokhimi, O. Novaro, R.D. Gonzalez, T. Lopez, O. Chimal, A. Asomoza, R. Gomez, , J. Solid State Chem., 144 (1999) 349-353.
4. B. Xia, H. Huang, Y. Xie, Mater. Sci. Eng. B, 57 (1999) 150-154.
5. K. Foger, J.R. Anderson, Appl. Catal., 23 (1986) 139-155.
6. J.M.G. Amores, V.S. Escribano, G. Busca, V. Lorezelli, J. Mater. Chem., 4 (1994) 965-971.
7. M.S.P. Francisco, V.R. Mastelaro, Chem. Mater., 14 (2002) 2514-2518.
8. S. Fukuji, H. Kazuaki, Y. Kazuaki, M. Yukio, T. Yoshitoma, J. Jpn Soc. Colour Mater., 79 (2006) 526-532.
9. A. Fujishima, X. Zhong, D.A. Tryk, Sci. Rep., 63 (2008) 515-582.
10. H.Y. Li, Y.F. Chen, C.X. Ruan, W.M. Gao, Y.S. Xie, J. Nano Part. Res., 3 (2001) 157-160.
11. T. Xu, C.S. Xie, Prog. Org. Coat., 46 (2003) 297-301.
12. N.S. Allen, M. Edge, A. Ortega, G. Sandoval, C.M. Lianw, J. Veeran, J. Stratton, R.B. McIntyre, Polym. Degrad. Stab., 3 (2004) 927-946.
13. L. Diamandesan, F. Vasillin, D.T. Mihaita, M. Fedar, A.M. Vlaicu, C.M. Teodorescu, D. Macuvei, I. Enculescu, V. Parvulescu, E. Vasile, Mater. Chem. Phys., 112 (2008) 146-153.
14. H. Shi, F. Liu, L. Yang, E. Han, Prog. Org. Coat., 62 (2008) 359-368.
15. A.M.K. Kirubaharan, M. Selvaraj, K. Maruthan, D. Jeyakumar, J. Coat. Technol. Res., 9 (2012) 163-170.
16. D.R. Coronado, G.R. Gattorno, M.E.E. Pesqueira, C. Cab, R. deCoss, G. Oskam, Nanotechnology, 19 (2008)145605.
17. I.B. Troitskaia, T.A. Gavrilova, V.V. Atuchin, Physics Procedia, 23 (2012) 65-68.
18. T.K. Kim, E.D. Jeong, M.S. Lee, J.P. Kim, M.H. Hyun, O.S. Jung, H. Suh, F. N. Khan, Res. Chem. Intermed., 38 (2012) 685-692.
19. J.G. Serrano, E.G. Hernandez, M.O. Fernandez, U. Pal, Curr. Appl. Phys., 9 (2009) 1097-1105.
20. N. Wetchakun, S. Phanichphant, Curr. Appl. Phys., 8 (2008) 343-346.
21. D. Bin Feng, Investigation of structural and magnetic properties of Ni implanted rutile, Sci. China-Phys. Mech. Astron., 55 (2012) 247-251.
22. B. Liang, S. Mianxin, Z. Tianliang, Z. Xiaoyong, D. Qingqing, J. Rare Earths, 27 (2009) 461-468.
23. H. Qiao, Q. Luo, Q. Wei, Y. Cai, F. Huang, Ionics, 18 (2012) 667-672.
24. Y. Zhang, S. Li, F. Huang, F. Wang, W. Duan, J. Li, Y. Shen, A. Xie, Russ. J. Physical Chem. A, 86 (2012) 413-417.
25. M. Omote, H. Kitaoka, E. Kobayashi, O. Suzuki, K. Aratake, H. Sano, G. Mizutani, W. Wolf, R. Podloucky, J. Phys. Condens. Matter, 17 (2005) S175-S200.
26. P. Praveen, G. Viruthagiri, S. Mugundan, N. Shanmugam, Spectrochim. Acta A, 117 (2014) 622-629.
27. P. Praveen, G. Viruthagiri, S. Mugundan, N. Shanmugam, Spectrochim. Acta A, 120 (2014) 548-557.
28. G. Viruthagiri, P. Praveen, N. Shanmugam, S. Mugundan, Preparation, Int. J. Curr. Res., 5 (2013) 2836-2839.
29. B. Rajamannan, S. Mugundan, G. Viruthagiri, P. Praveen, N. Shanmugam, Spectrochim. Acta A, 118 (2014) 651-656.
30. B. Rajamannan, S. Mugundan, G. Viruthagiri, N. Shanmugam, P. Praveen, Properties of sol-gel derived Silver doped Titania nanoparticles, Int. J. Curr. Res., 5 (2013) 2863-2867.

31. B. Rajamannan, S. Mugundan, G. Viruthagiri, N. Shanmugam, R. Gobi, P. Praveen, Spectrochim. Acta A, 128 (2014) 218-224.
32. S. Mugundan, B. Rajamannan, G. Viruthagiri, N. Shanmugam, R. Gobi, P. Praveen, Appl. Nanosci., (2014), DOI: 10.1007/s13204-014-0337-y.
33. N. Khakpash, A. Simchi, T. Jafari, J. Mater. Sci: Mater. Electron., 23 (2012) 659-667.
34. D. Zhang, Russ. J. Phys. Chem. A, 86 (2012) 489-494.
35. R. Chauhan, A. Kumar, R.P. Chaudhary, J. Sol-Gel Sci. Technol., 61 (2012) 585-591.
36. R. Suresh, V. Ponnuswamy, R. Mariappan, Appl. Surf. Sci., 273 (2013) 457-464.
37. C. Chen, P. Liu, C. Lu, Chemical Engineering Journal, 144 (2008) 509-513.
38. A.S. Edelestein, R.C. Camarata, Nanomaterials Synthesis Properties and Application, Institute of Physics Publishing, CRC Science, 1998, pages-616.
39. J.M. Needeljkovic, A.C. Patel, P. Kaufman, O. Leary, J. Chem. Educ., 70 (1993), DOI: 10.1021/ed070p342.
40. P.A. Sant, P.V. Kamat, Phys. Chem. Chem. Phys., 4 (2002) 198-203.
41. Z. Sui, X. Chen, L. Wang, Chem. Lett., 34 (2005) 100-101.
42. A. Kathiravan, R. Renganathan, J. Colloid Interface Sci., 335 (2009) 196-202.
43. J.C. Xu, Y.L. Shi, J.E. Huang, B. Wang, H.L. Li, J. Mol. Catal. A: Chem., 219 (2004) 351-355.
44. H.J. Zhai, L. S. Wang, J. Am. Chem. Soc., 129 (2007) 3022-3026.
45. W. Zhao, Z. Bai, A. Ren, B. Guo, C. Wu, Appl. Surf. Sci., 256 (2010) 3493-3498.
46. G. Blasse, B.C. Grabmaier, Luminescent materials, Springer-Verlag, Berlin, 1994, DOI: 10.1007/978-3-642-79017-1.
47. H. Lin, C.P. Huang, W. Li, C. Ni, S. Ismat Shah, Y.H. Tseng, Appl. Catal. B: Environ., 68 (2006)1-11.
48. P. Prathap, Y.P. Subaiah, M. Devika, K.T. Ramakirushna Reddy, Mater. Chem. Phys., 100 (2006) 375-379.
49. D. Beena, K.J. Lethy, R. Vinodkumar, V.P. Mahadevan Pillai, V. Ganesan, D.M. Phase, S.K. Sudheer, Appl. Surf. Sci., 255 (2009) 8334-8342.
50. M.R. Islam, J. Podder, Res. Technol., 44 (2009) 286-292.
51. M.A.M. Khan, M.W. Khan, M. Alhoshan, M.S. Alsalhi, A.S. Aldwayyan, Appl. Phys. A, 100 (2010) 45-51.
52. F. Yakuphanoglu, S. Ilican, M. Caglar, Y. Caglar, J. Optoelectron. Adv. Mater., 9 (2007) 2180-2185.
53. M. Sesha Reddy, K.T. Ramakrishna Reddy, B.S. Naidu, P.J. Reddy, Opt. Mater., 4 (1995) 787-790.
54. J.I. Pankove, Optical Processes in Semiconductors, Prentice-Hall, New Jersey, 1971, pages-92.